Geophysical Research Letters

Supporting Information for

Constraining Fault Friction and Stability with Fluid-Injection Field Experiments

Stacy Larochelle[1], Nadia Lapusta[1,2], Jean-Paul Ampuero[3], and Frédéric Cappa[3,4]

[1] Division of Geological and Planetary Sciences, California Institute of Technology, Pasadena, California 91125, USA.
[2] Division of Engineering and Applied Science, California Institute of Technology, Pasadena, California 91125, USA
[3] Université Côte d'Azur, IRD, CNRS, Observatoire de la Côte d'Azur, Géoazur, 06560 Sophia Antipolis, France
[4] Institut Universitaire de France, Paris, France

Contents of this file

Introduction

The following supporting information offers further details on the numerical model and its assumptions as well as derivations of simple formulations and additional figures that illustrate how certain combinations of parameters control the simulation results.

Text S1. Numerical modeling of fluid-induced fault slip

We model fluid injection into a fault zone and subsequent fault slip using a fully-dynamic 2D boundary integral method capable of simulating the complete seismic cycle including both aseismic and seismic deformation. The model is based on an antiplane (Mode III) formulation in which the fault slips solely along the dip direction and variables vary along strike only. Fault slip is governed by the following elastodynamic equation (Lapusta et al., 2000):

$$\tau(x,t) = \tau_{ini} + F(\delta(x,t)) - \frac{\mu}{2c_s} V(x,t) \tag{S1}$$

where τ is the shear stress, τ_{ini} is the initial shear stress, F is a linear functional which depends on the slip history, $\delta(x,t)$, μ is the shear modulus of the elastic medium, c_s is the shear wave speed, and V is the slip rate.

The fault is governed by rate-and-state friction, an empirical friction law based on laboratory experiments. It describes the dependence of the coefficient of friction f on the slip rate V and a state variable θ:

$$f(V(x,t),\theta(x,t)) = \left[f^* + a \ln \frac{V(x,t)}{V^*} + b \ln \frac{V^* \theta(x,t)}{D_{RS}} \right] \tag{S2}$$

where a and b are the direct and evolutionary rate-and-state parameters and D_{RS} is the critical slip distance. f^* is the reference coefficient of friction at the reference slip rate V^*. The reference values are usually set arbitrarily but here, by choosing V^* to be on the order of the slip rate observed during the accelerated aseismic transient in the field experiment, we attach the following additional meaning to the value of f^*: it is approximately equal to the residual friction reached at the latest stage of the field experiment.

The state variable is assumed to evolve according to the aging law:

$$\frac{\partial \theta(x,t)}{\partial t} = 1 - \frac{V(x,t)\theta(x,t)}{D_{RS}} \tag{S3}$$

We prescribe the fluid pressure at the center of the fault (blue line in Figure 2A, top) similar to the one induced in the field experiment (black dots in Figure 2A, top) to

simulate the fluid injection and let the pressure diffuse axisymmetrically in the fault plane as follows:

$$\frac{\partial p(r,t)}{\partial t} = \alpha\left(\frac{\partial^2 p(r,t)}{\partial r^2} + \frac{1}{r}\frac{\partial p(r,t)}{\partial r}\right) \quad \text{(S4)}$$

where $r = |x|$ and α hydraulic diffusivity. The diffusion is numerically implemented using a forward finite difference scheme. We approximate the experimental injection pressure with a smooth parabolic function for the increasing portion of the injection and a linear fit for the decreasing portion. A condition of zero pressure is assumed at the ends of the simulated fault since the fault is dry prior to the injection. The choice of this boundary condition is not essential here because the fault length is larger than the pressure diffusion length in our simulations and simulations with longer faults produce nearly identical results.

As the fault in the experiment is inactive prior to the fluid stimulation, the modeled fault is not loaded tectonically. Fault slip is thus purely fluid-induced, i.e., no significant slip would occur without the injection within the time scales considered in the simulations. We prescribe initial conditions that are consistent with a dormant fault by starting with a highly healed fault (i.e., high initial value of the state variable θ_{ini}). This choice of initial conditions is justified by the long-term simulations without tectonic or fluid pressure loading shown in Figures S1 to S4. The initial values affect some initial behavior/slip of the fault but, long-term, the fault heals under the near-constant values of shear stress, with a power-law decrease in slip rate as well as an increase in state variable over time; at long times, the value of the state variable is approximately equal to the healing time of the fault. This behavior can be predicted analytically: When the fault is well below steady-state ($V\theta/D_{RS} \ll 1$), $\dot{\theta} \sim 1$ and thus $\theta \sim t$. Moreover, with shear stress being almost constant, the rate-and-state friction coefficient is fixed and $\dot{f} = a\dot{V}/V + b/t = 0$, implying that $V \propto t^{-b/a}$. The initial conditions in the intermediate- and high-friction cases in this study are consistent with this behavior. In the low-friction case, although we do prescribe a high initial state variable and a low initial slip rate, the fault needs to be initially above steady state to match the measured

slip behavior at the injection size and therefore not consistent with the behavior described above.

Finally, we also test the effect of the domain size in Figure S5. Increasing the domain size slightly changes the timing of earthquakes but not the overall behavior.

Text S2. Controlling the timing of slip initiation and acceleration

The slip measured at the injection site of the field experiment displays two distinct slip stages that we aim to reproduce in our simulations. Stage I starts when slip rates attain ~10^{-7} m/s and significant slip initiates, at about 400 s. Stage II is characterized by even higher slip velocities of about ~10^{-6} m/s, at about ~1200 s. Understanding how the different model parameters govern the onsets of Stages I and II is key to arriving at simulations that replicate the observations.

At the beginning of all simulations, slip rates are low and inertial effects are negligible. Eq. S1 and S2 then reduce to:

$$\tau_{ini} = f(x,t)[\sigma - p(x,t)] \tag{S5}$$

As p is increased, the friction coefficient, f, must increase proportionally for Eq. S5 to remain true since τ_{ini} stays constant over time and the contribution of F is negligible because no significant slip has occurred yet. The coefficient of friction continues increasing until slip becomes significant. The onset of significant slip thus approximately coincides with the maximum friction reached during the simulation. This peak friction, f^p, can be approximated as:

$$f^p = f^* + a\ln\frac{V_s}{V^*} + b\ln\frac{V^*\theta_{ini}}{D_{RS}} \tag{S6}$$

where V_s is the threshold for significant slip, here set at 1e-7 m/s. The state variable is set to its initial value, θ_{ini}, because it cannot evolve significantly due to lack of slip, and its (large) initial value is not affected by additional healing over hundreds of seconds. Moreover, because the shear stress τ remains approximately constant and equal to the initial value until the peak friction is reached and the fluid pressure at the injection site is known at all times, it is possible to relate f^p to the timing of slip initiation. For

example, for slip initiation at t_s = 300 s - at which point the injection fluid pressure is 1.42 MPa - the peak friction at the injection site is:

$$f^p = \frac{\tau_{ini}}{[\sigma - p(0,t_s)]} = \frac{2.15}{[4.00 - 1.42]} = 0.83 \quad \text{(S7)}$$

It is thus possible to control t_s by computing f^p with Eq. S7 and selecting f^*, a, b, θ_{ini} and D_{RS} such that Eq. S6 is satisfied.

We find that the onset time, t_{ac}, of the slip acceleration starting at ~1200 s (i.e., Stage II) coincides with the time at which steady state is reached at the injection site (Dublanchet, 2019). This also corresponds to the time at which the coefficient of friction at the injection site reaches its residual value, $f^r \sim f^*$, down from its peak value f^p. The critical slip distance, δ_c, over which this frictional weakening occurs can be approximated as:

$$\delta_c \sim \frac{f^p - f^*}{b/D_{RS}} \quad \text{(S8)}$$

since $\frac{\partial f}{\partial \delta} \sim \frac{b}{D_{RS}}$. Furthermore, from elasticity, slip is related to stress drop by:

$$\Delta\delta \propto \frac{\Delta\tau h}{\mu} \quad \text{(S9)}$$

where h is the length of the slipping zone. When $\Delta\delta = \delta_c$ at the center of the fault:

$$\frac{\Delta\tau h}{\mu} \propto \frac{f^p - f^*}{b/D_{RS}} \quad \text{(S10)}$$

Rearranging Eq. S10, we can find the estimate of the slipping zone size, h_{ac}, at which steady state is reached and Stage II is initiated:

$$h_{ac} \propto \frac{\mu\, D_{RS}}{b} \frac{f^p - f^*}{\Delta\tau} \quad \text{(S11)}$$

Eq. S11 can be rewritten in terms of known parameters as:

$$h_{ac} \propto \frac{\mu\, D_{RS}}{b} \frac{a \ln \frac{V_s}{V^*} + b \ln \frac{V^* \theta_{ini}}{D_{RS}}}{\tau_{ini} - f^*[\sigma - p(0,t_{ac})]} \quad \text{(S12)}$$

For all the simulations presented in this work, we find that

$$h_{ac} = 3\frac{\mu\, D_{RS}}{b}\frac{a \ln \frac{V_s}{V^*} + b \ln \frac{V^* \theta_{ini}}{D_{RS}}}{\tau_{ini} - f^*[\sigma - p(0,\, t_{ac})]} \quad \text{(S13)}$$

provides a good estimate of the slipping zone length at which the slip transitions to Stage II. Note that if $(\sigma - p)$ remained constant throughout the simulation, Eq. S11 would reduce to $h_{ac} \propto \mu D_{RS}/b$ which is similar to the condition for acceleration $k < k_b$ (where k is stiffness) in the spring-block slider model (Dieterich, 1992; Helmstetter & Shaw, 2009) and to the condition $h > L_b$ for acceleration on continuum fault segments that are far above steady-state (Rubin & Ampuero, 2005). Eq. S11 is also similar to the findings for seismic slip nucleation in slip-weakening friction models (Uenishi & Rice, 2003; Viesca & Rice, 2012) except that h_{ac} depends on pressure; specifically on the maximum value of pressure (at the injection site). The fact that this lengthscale does not depend - at least to first order - on the extent or shape of the pore pressure distribution is also consistent with prior findings (Uenishi & Rice, 2003; Viesca & Rice, 2012). At the same time, h_{ac} is different from some of the discussed critical lengthscales, since it does not signify the transition to dynamic, inertially-controlled earthquake slip, but rather corresponds to the beginning of the different quasi-static slip stage in this particular experiment. The existence of h_{ac} is linked to the two-stage quasi-static slip process in the field experiment which the simulations are trying to emulate. The associated evolution of the friction coefficient - with sharp increase to a peak value, then near-linear decrease vs. slip with the slope of b, and then near-constant value - is likely related to the relatively rapid increase of the pore pressure at the injection site compared to the timescale of state variable evolution considered in this work.

To demonstrate that Eq. S13 holds, in Figures S12(A-C) and S13 we show 3 simulations in which h_{ac} is increased compared to the intermediate-friction case by increasing μ (pink), increasing D_{RS} (yellow) or decreasing b (turquoise) while keeping t_s constant. Figures S12(D-E) and S14 show simulations in which both t_s and h_{ac} are increased by increasing f^*(pink) or θ_{ini} (yellow). Figures S12(F) and S14 also show a case (turquoise) in which both t_s and h_{ac} are kept the same as in the intermediate-friction

reference case but t_{ac} is delayed due to the decreased hydraulic diffusivity α which controls how fast the slipping zone expands during Stage I. In all cases, the onset of Stage II is delayed compared to the intermediate-friction reference case. Thus, parameters μ, D_{RS}, b, t_s and α have a primary control on the onset of Stage II observed in all simulations shown in this work.

As for the amplitude and slope of the slip acceleration, four parameters - f^*, a, μ and α - have been identified to play a key role in controlling them as shown in Figures S15 to S19.

Table S1. Model parameters for the three cases presented in Figures 2-4 in the main text.

Properties	**Symbol**	**Low Friction**	**Intermediate Friction**	**High Friction**
Total fault length [m]	x_{tot}	250	250	250
Frictional interface length [m]	x_{fr}	200	200	200
Initial shear stress [MPa]	τ_{ini}	2.15	2.15	2.15
Initial normal stress [MPa]	σ_{ini}	4.00	4.00	4.00
Initial coefficient of friction	f_{ini}	0.5375	0.5375	0.5375
Reference coefficient of friction	f^*	0.4815	0.5500	0.6000
Reference slip rate [m/s]	V^*	10^{-6}	10^{-6}	10^{-6}
Direct effect frictional parameter	a	0.01500	0.01125	0.01125
Evolutionary effect frictional parameter	b	0.01600	0.01600	0.01600
Critical slip distance [μm]	D_{RS}	16.75	16.75	16.75
Hydraulic diffusivity [m^2/s]	α	0.04	0.20	0.85
Initial state variable [s]	θ_{ini}	1.21e12	2.38e12	7.00e12
Shear modulus [GPa]	μ	10	10	10

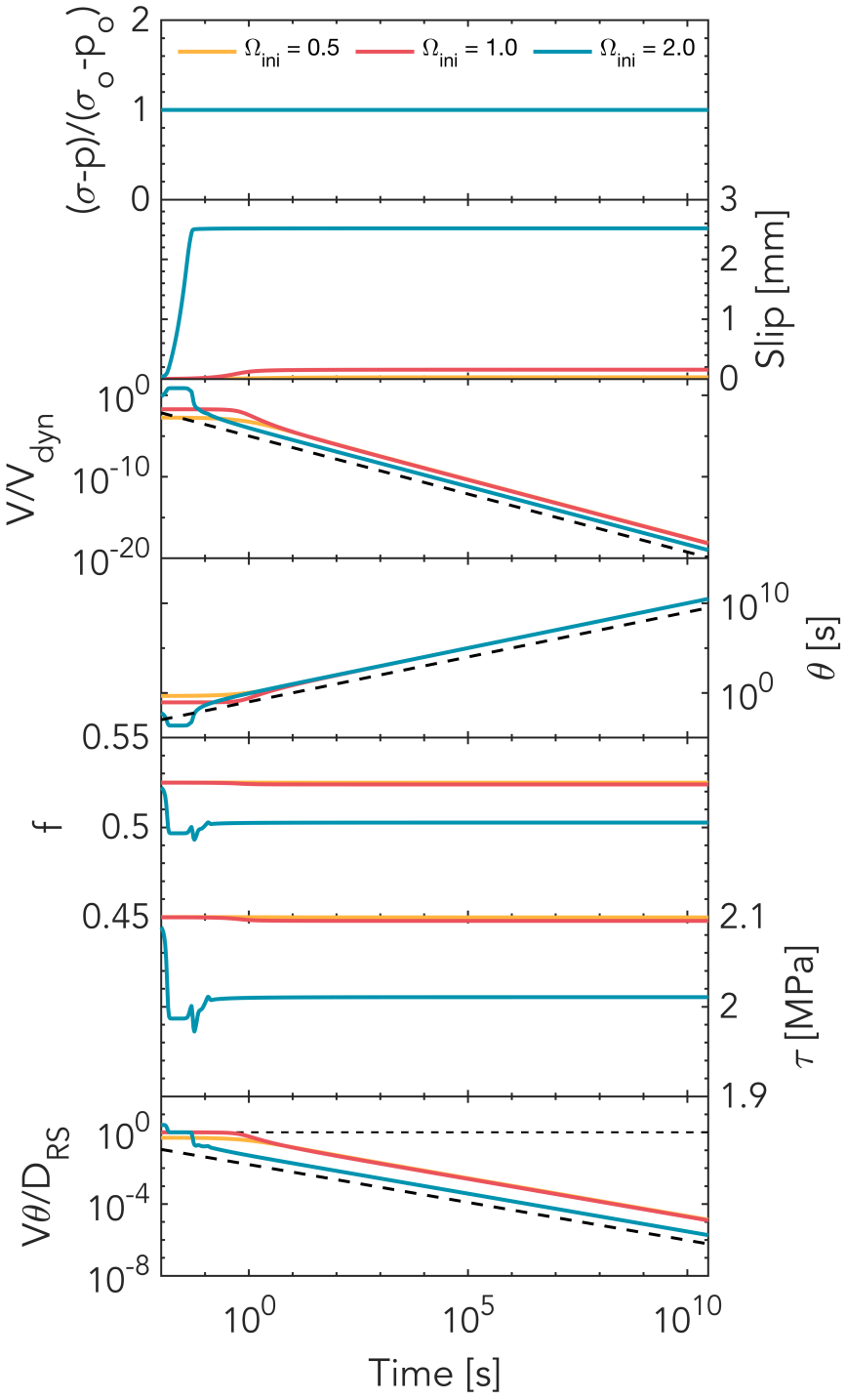

Figure S1. Simulations that illustrate long-term fault healing in the absence of slip, with f^* = 0.550, f_{ini} = 0.525, a = 0.011, and b = 0.016, varying the initial closeness to steady state ($\Omega_{ini} = V_{ini}\theta_{ini}/D_{RS}$). No matter what the initial values are, all cases eventually undergo a logarithmic decrease in slip rate and an increase in state variable with time. Note that the time axis is logarithmic. The thick dashed lines indicate the slopes discussed in the Text S1.

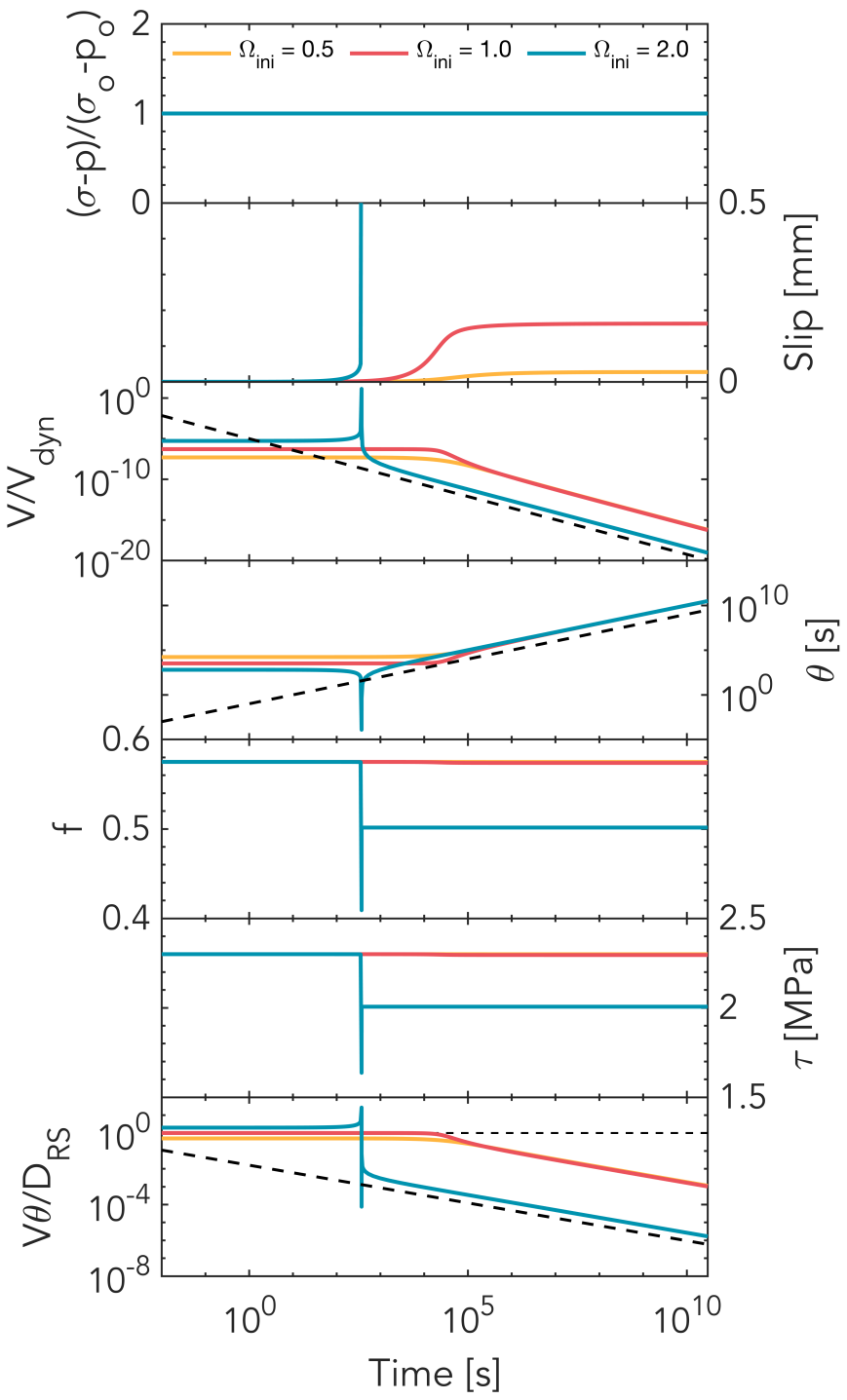

Figure S2. Simulations that illustrate long-term fault healing in the absence of slip, with f^* = 0.550, f_{ini} = 0.575, a = 0.011, and b = 0.016, varying the initial closeness to steady state ($\Omega_{ini} = V_{ini}\theta_{ini}/D_{RS}$). No matter what the initial values are, all cases eventually undergo a logarithmic decrease in slip rate and an increase in state variable with time, even the initially above steady-state case which experiences a run-away earthquake a few minutes into the simulation. Note that the time axis is logarithmic. The thick dashed lines indicate the slopes discussed in Text S1.

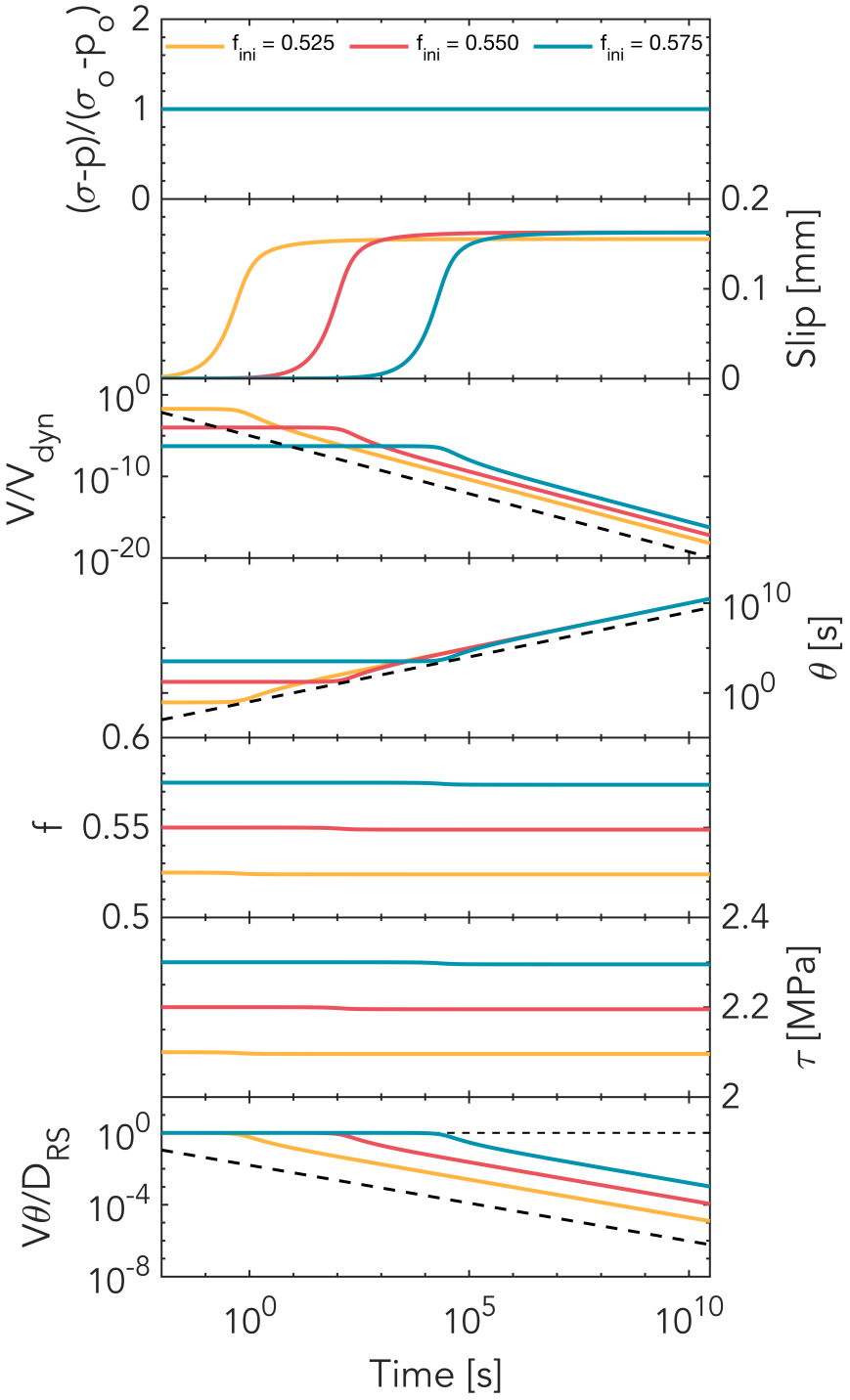

Figure S3. Simulations that illustrate long-term fault healing in the absence of slip, with f^* = 0.550, Ω_{ini} = 1, a = 0.011, and b = 0.016, varying the initial friction coefficient, f_{ini}. No matter what the initial values are, all cases eventually undergo a logarithmic decrease in slip rate and an increase in state variable with time. Note that the time axis is logarithmic. The thick dashed lines indicate the slopes discussed in Text S1.

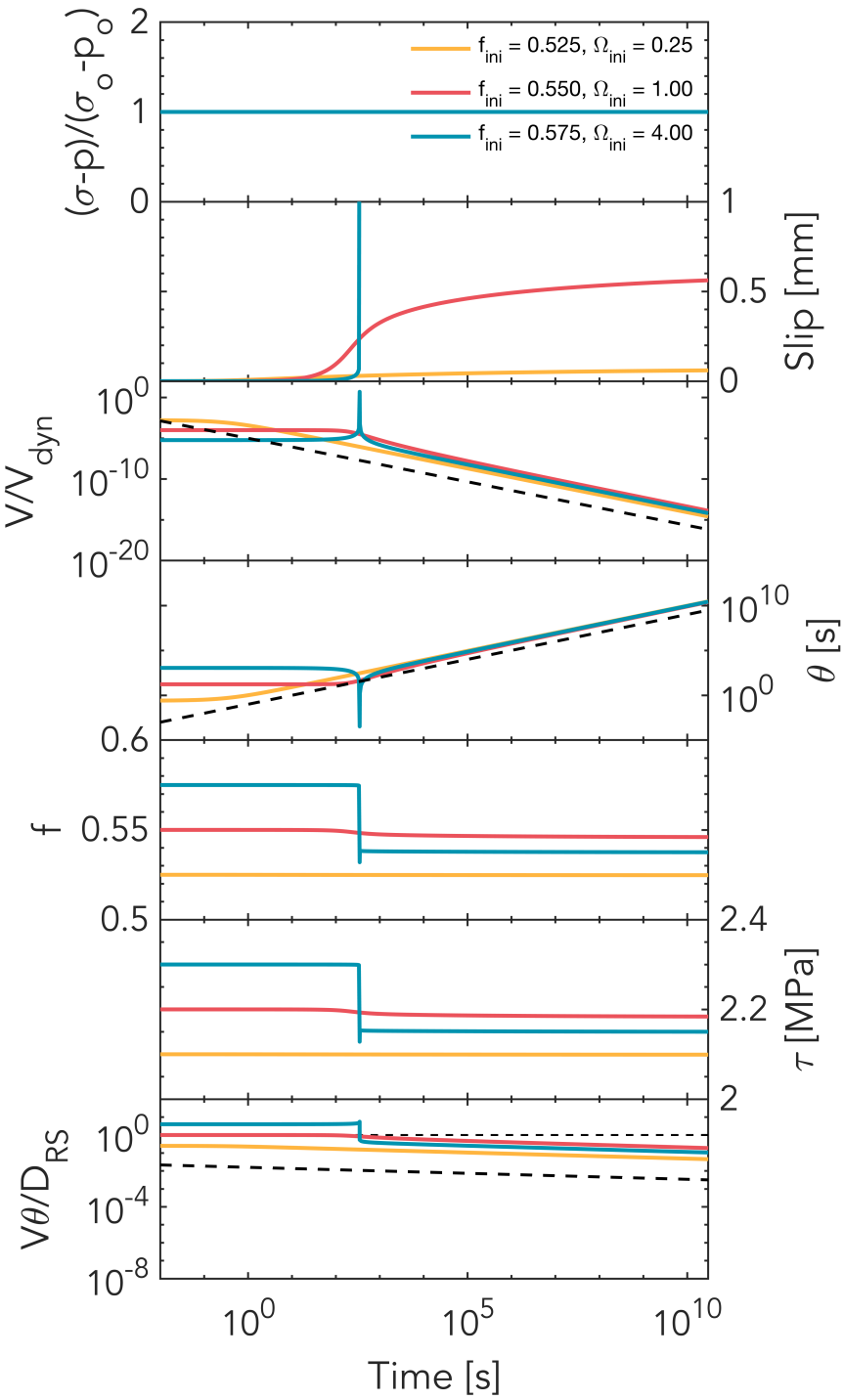

Figure S4. Simulations that illustrate long-term fault healing in the absence of slip, with f^* = 0.550, a = 0.015, and b = 0.016, varying the initial closeness to steady state ($\Omega_{ini} = V_{ini}\theta_{ini}/D_{RS}$) and initial friction coefficient f_{ini}. No matter what the initial values are, all cases eventually undergo a logarithmic decrease in slip rate and an increase in state variable with time, even the initially above steady-state case which experiences a run-away earthquake a few minutes into the simulation. Note that the time axis is logarithmic. The thick dashed lines indicate the slopes discussed in Text S1.

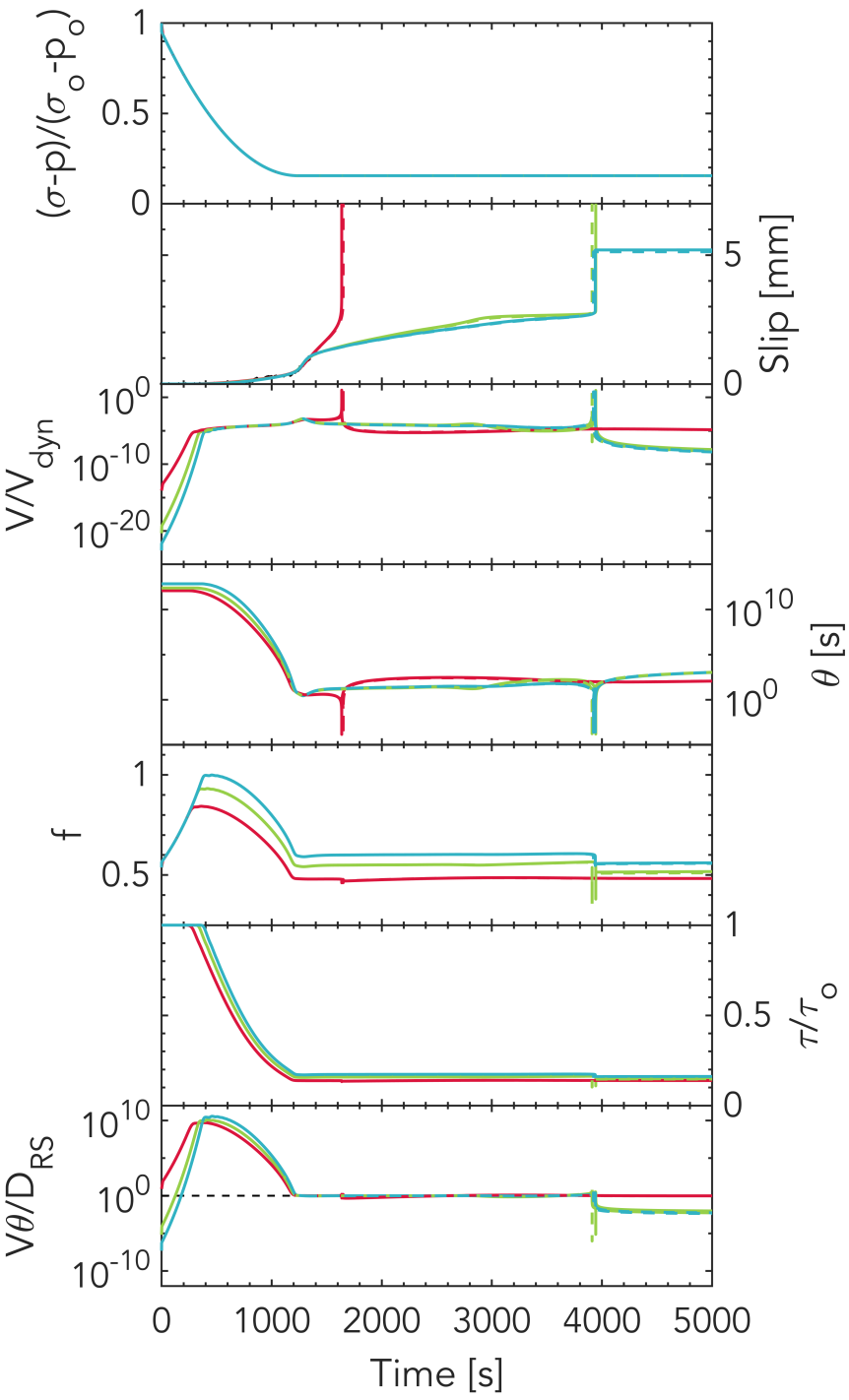

Figure S5. Prolonged injection simulations with domain sizes of 250 m (solid lines) and 300 m (dashed lines). Changing the domain size slightly changes the timing but not the overall behavior.

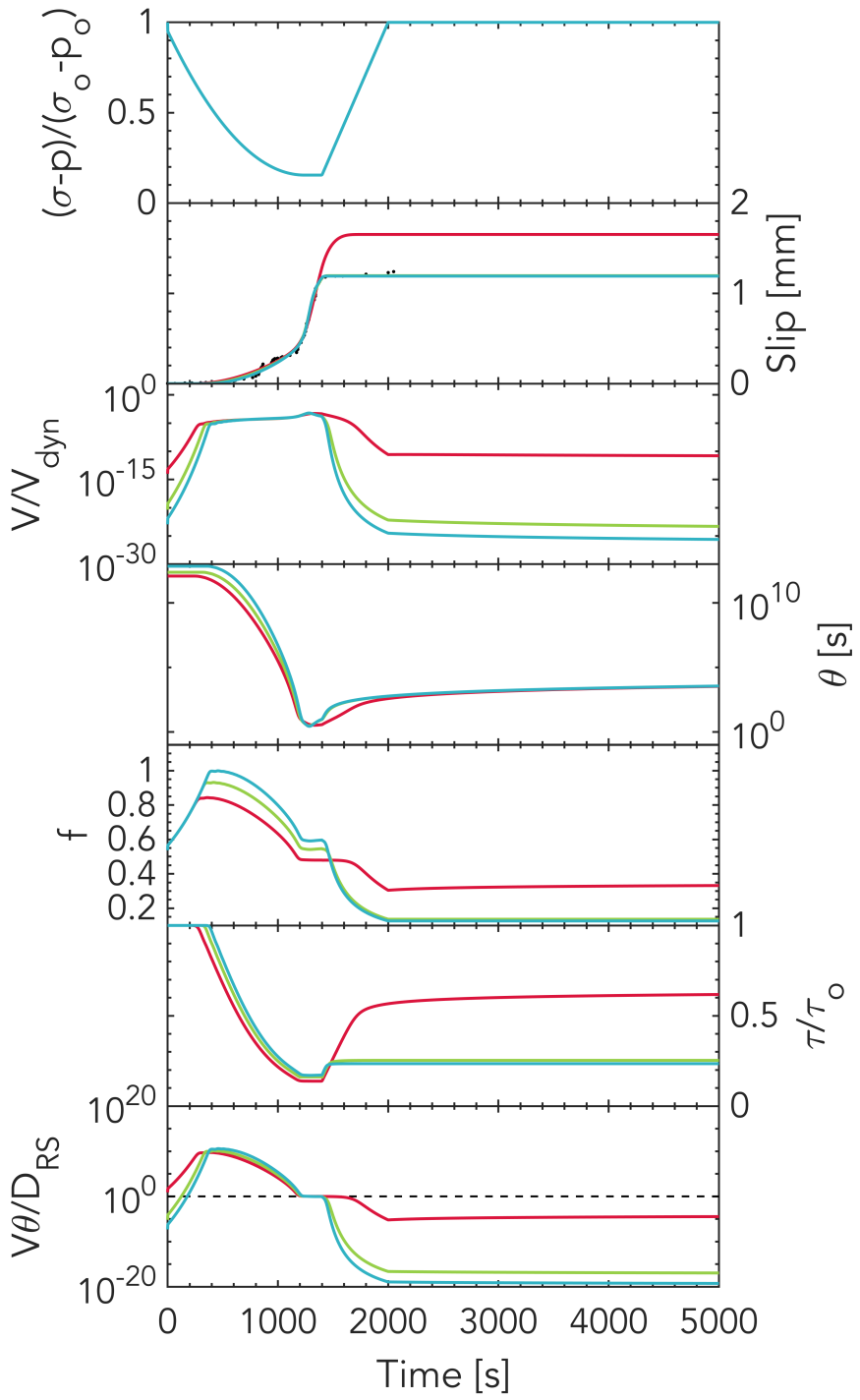

Figure S6. Simulated temporal evolution of several quantities at the injection site for the cases of Figure 2A in the main text. From top to bottom: the normalized effective normal stress, slip, normalized slip rate (V_{dyn} = 10^{-2} m/s), state variable, friction coefficient, normalized shear stress and closeness to steady state at the injection site. Note that no earthquakes occur in these simulations as opposed to cases in which the pressure is kept constant at the injection site (Figure 4 in the main text).

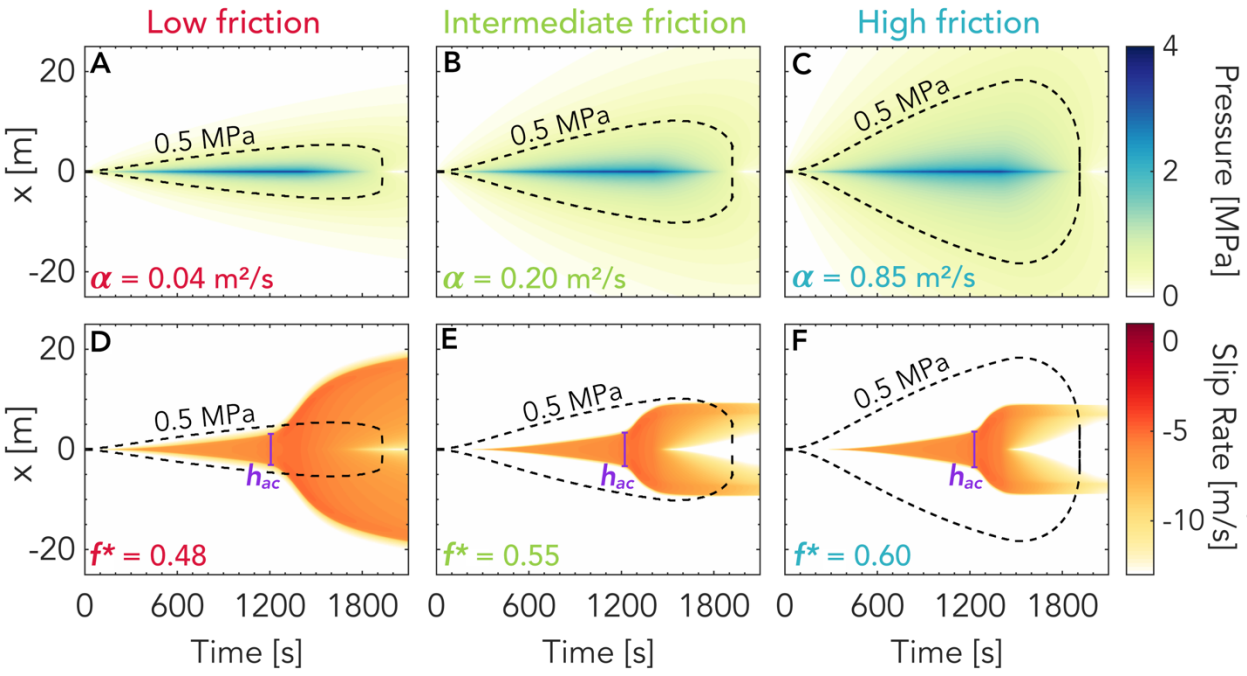

Figure S7. Same as Figure 3 in the main text but including the depressurization stage.

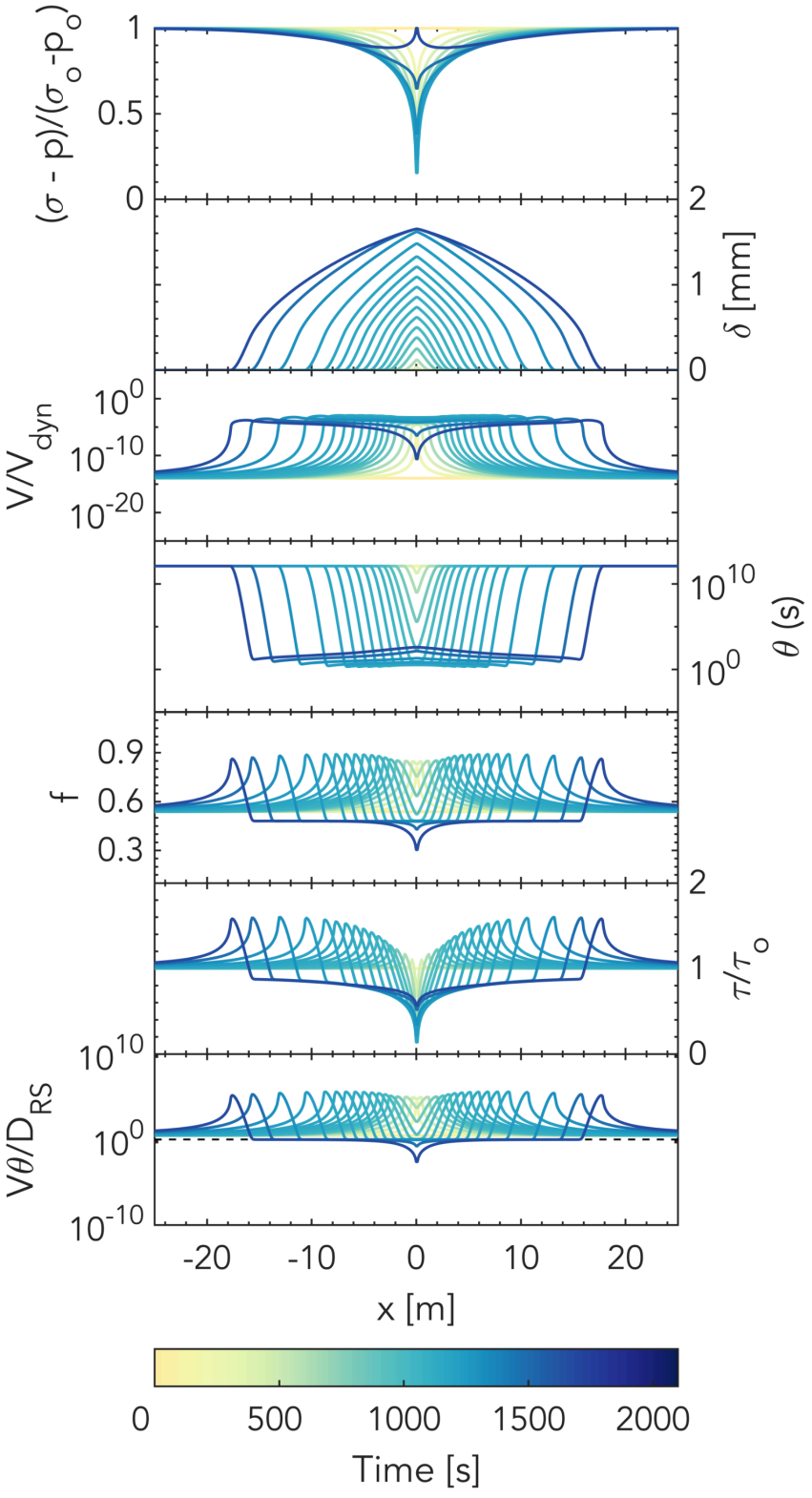

Figure S8. Spatial and temporal evolution of the same quantities as in Fig. S6 for the low-friction case (plotted every 2000 time steps).

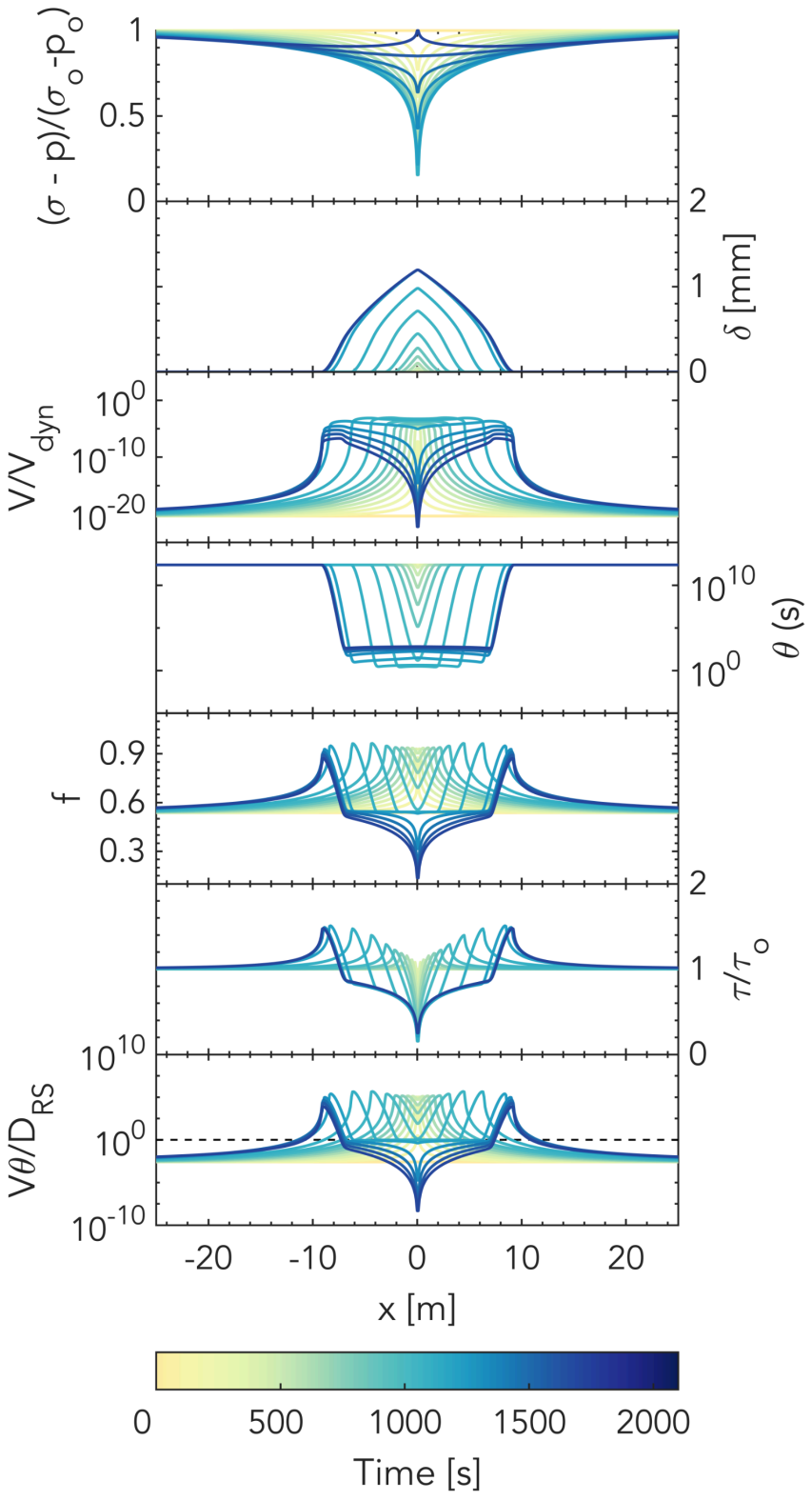

Figure S9. Spatial and temporal evolution of the same quantities as in Fig. S6 for the intermediate-friction case (plotted every 6000 time steps).

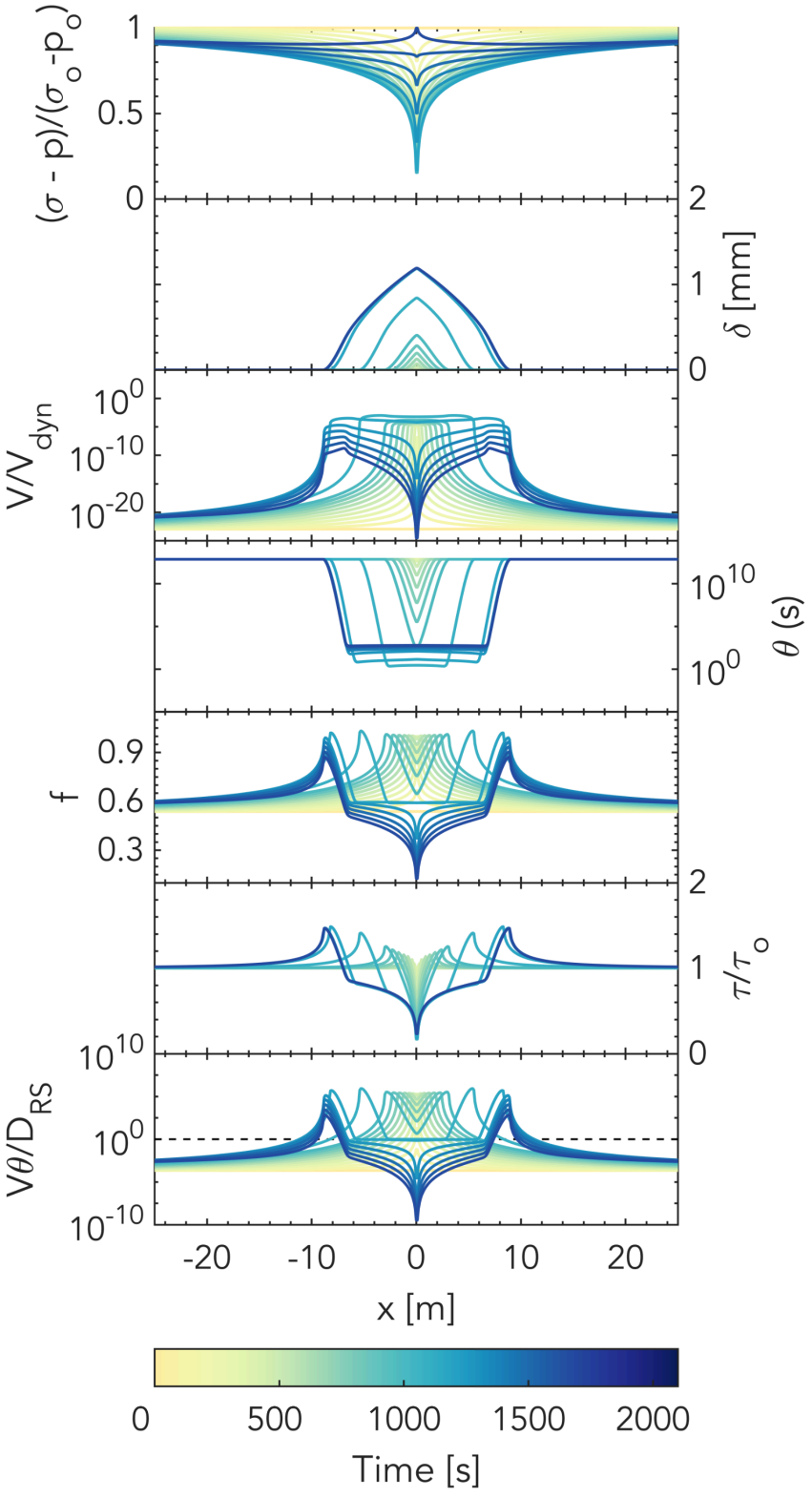

Figure S10. Spatial and temporal evolution of the same quantities as in Fig. S6 for the high-friction case (plotted every 20000 time steps).

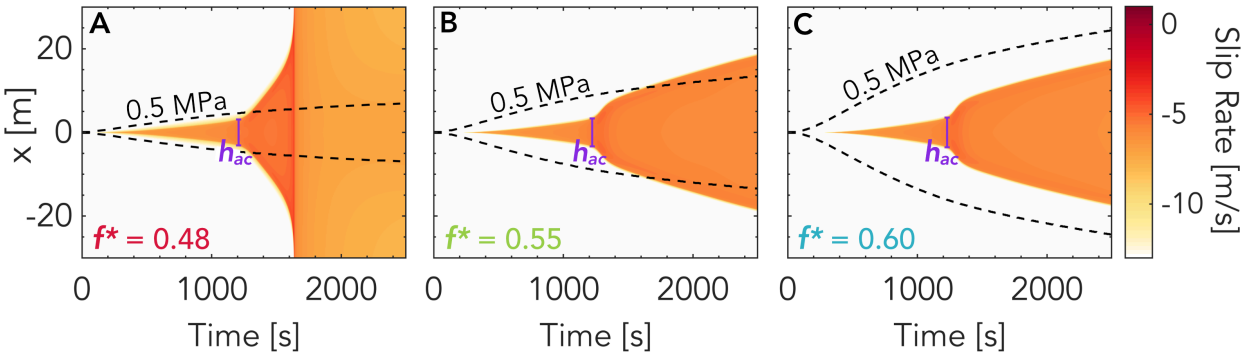

Figure S11. Same as Figure 4C-E in the main text but up to 2500s to enable direct comparison with Figures S12 and S19.

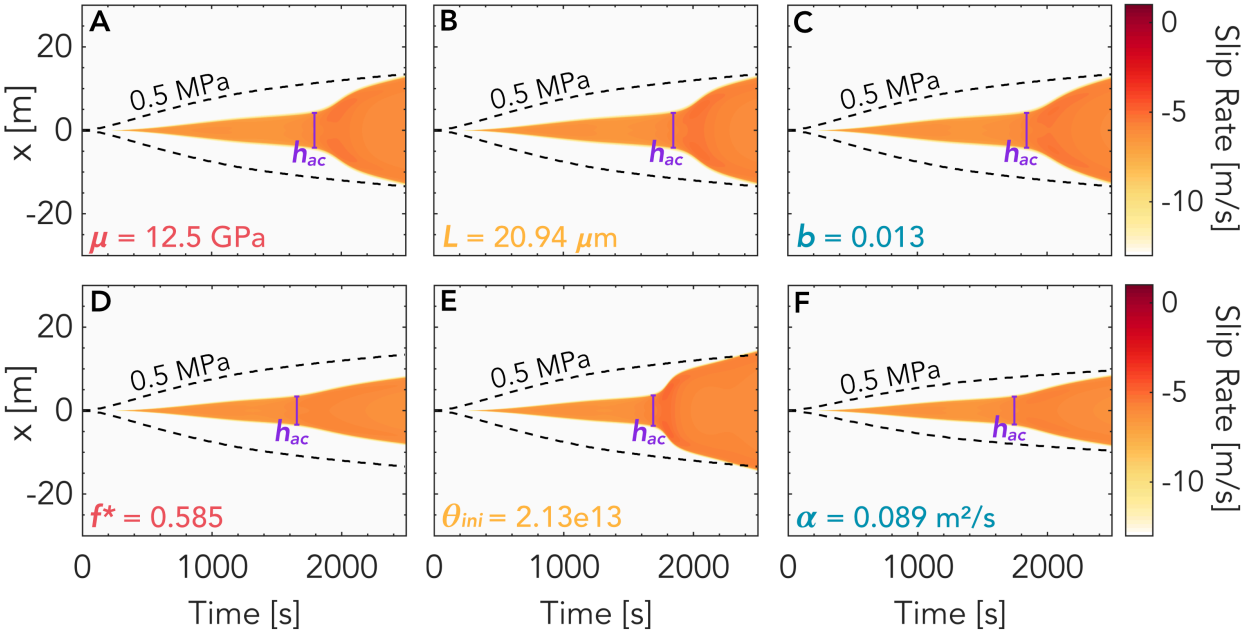

Figure S12. Spatial and temporal evolution of slip rate for prolonged injection (as in Figure S11) but for cases modified from the intermediate-friction case (Figure S11B) in which the onset of Stage II is delayed by (A) increasing μ, (B) increasing D_{RS}, (C) decreasing b, (D) increasing f^*, (E) increasing θ_{ini}, (F) decreasing hydraulic diffusivity α. Note that h_{ac} provides a good estimate of the extent of the sliding region before the onset of Stage II in all these cases.

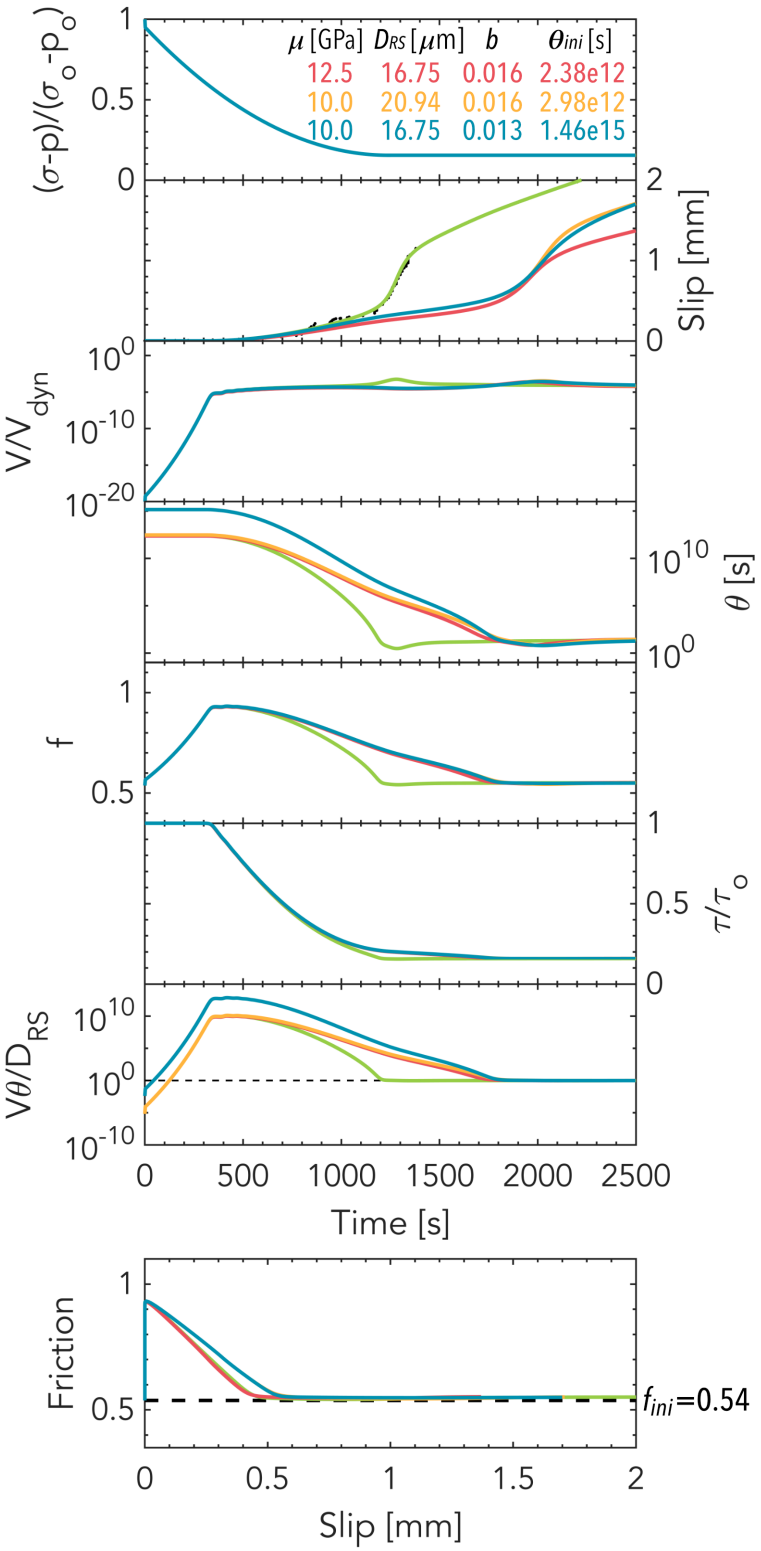

Figure S13. Temporal evolution of quantities at the injection site and friction vs. slip for the 3 cases shown in Figure S12(A-C) in which μ is increased (pink) or D_{RS} is increased (yellow) or b is decreased (turquoise) compared to the intermediate-friction reference case (green). Note the delay in the transient acceleration compared to the reference case.

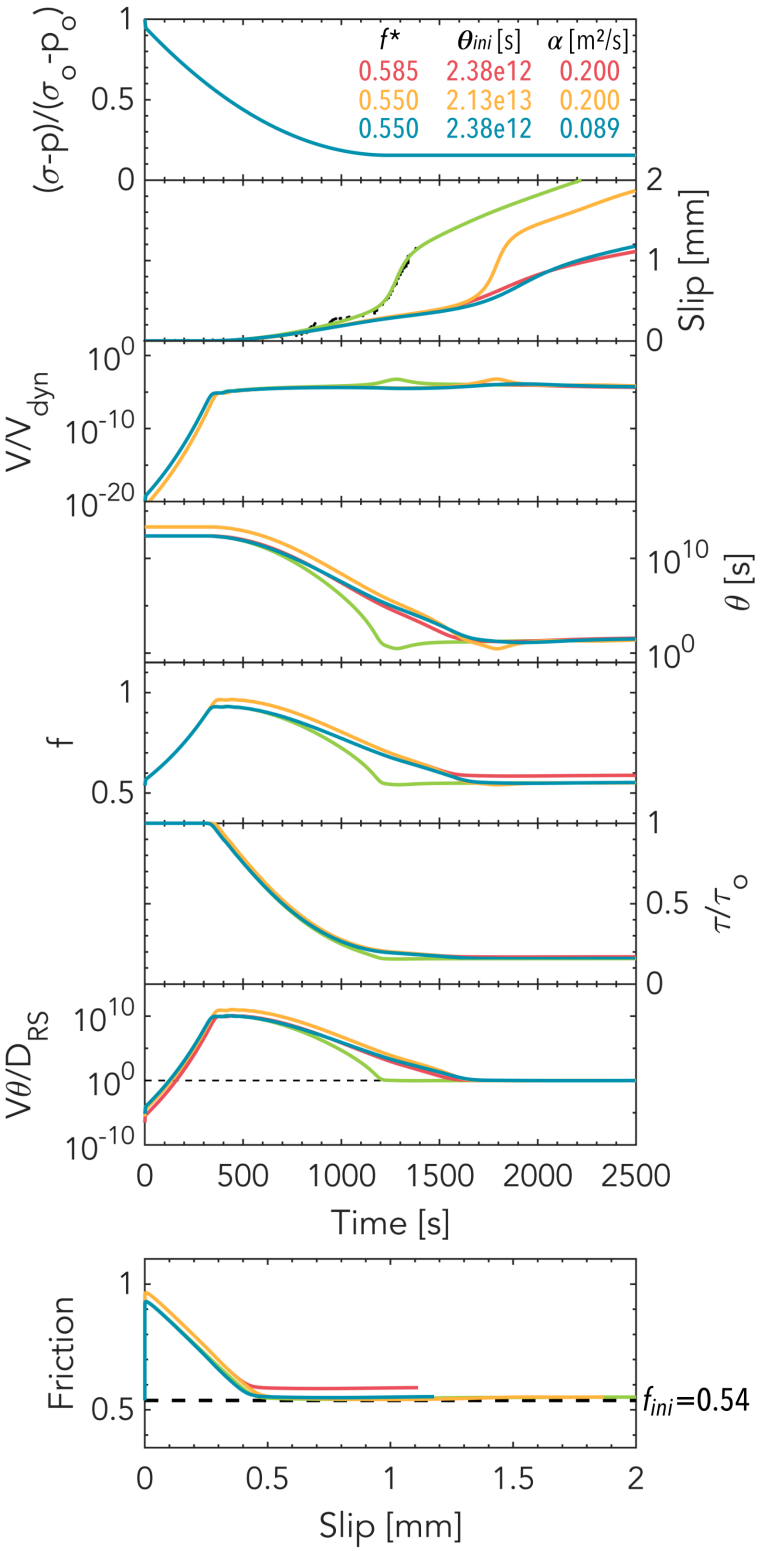

Figure S14. Temporal evolution of quantities at the injection site and friction vs slip for the 3 cases shown in Figure S12(D-F) in which f^* is increased (pink) or θ_{ini} is increased (yellow) or α is decreased (turquoise) compared to the intermediate-friction reference case (green). Note the delay in the transient acceleration compared to the reference case.

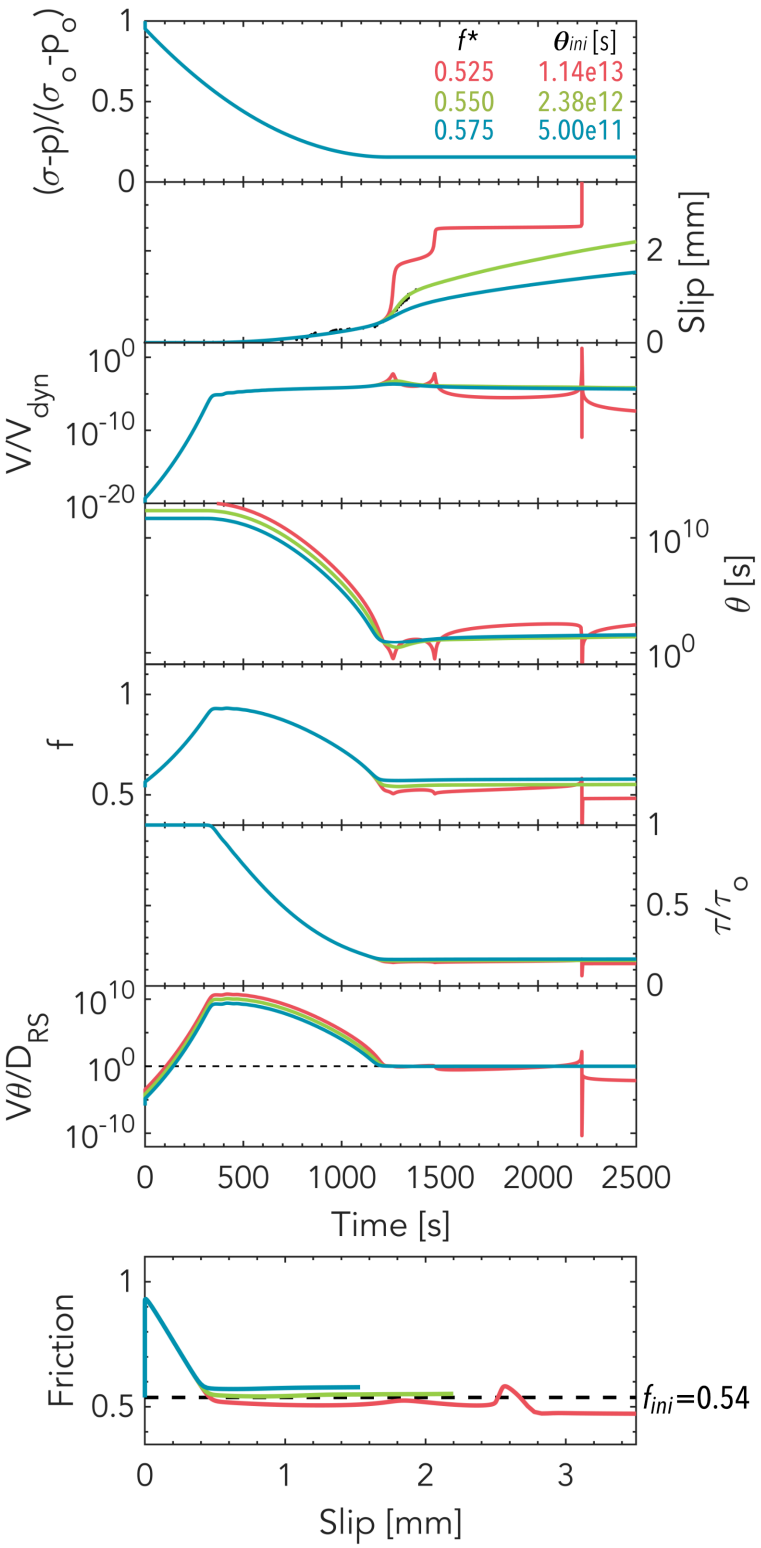

Figure S15. Temporal evolution of quantities at the injection site and friction vs slip of 2 cases showing the effect of varying f^* while keeping f^p constant. Increasing f^* reduces the amplitude and slope of the transient acceleration.

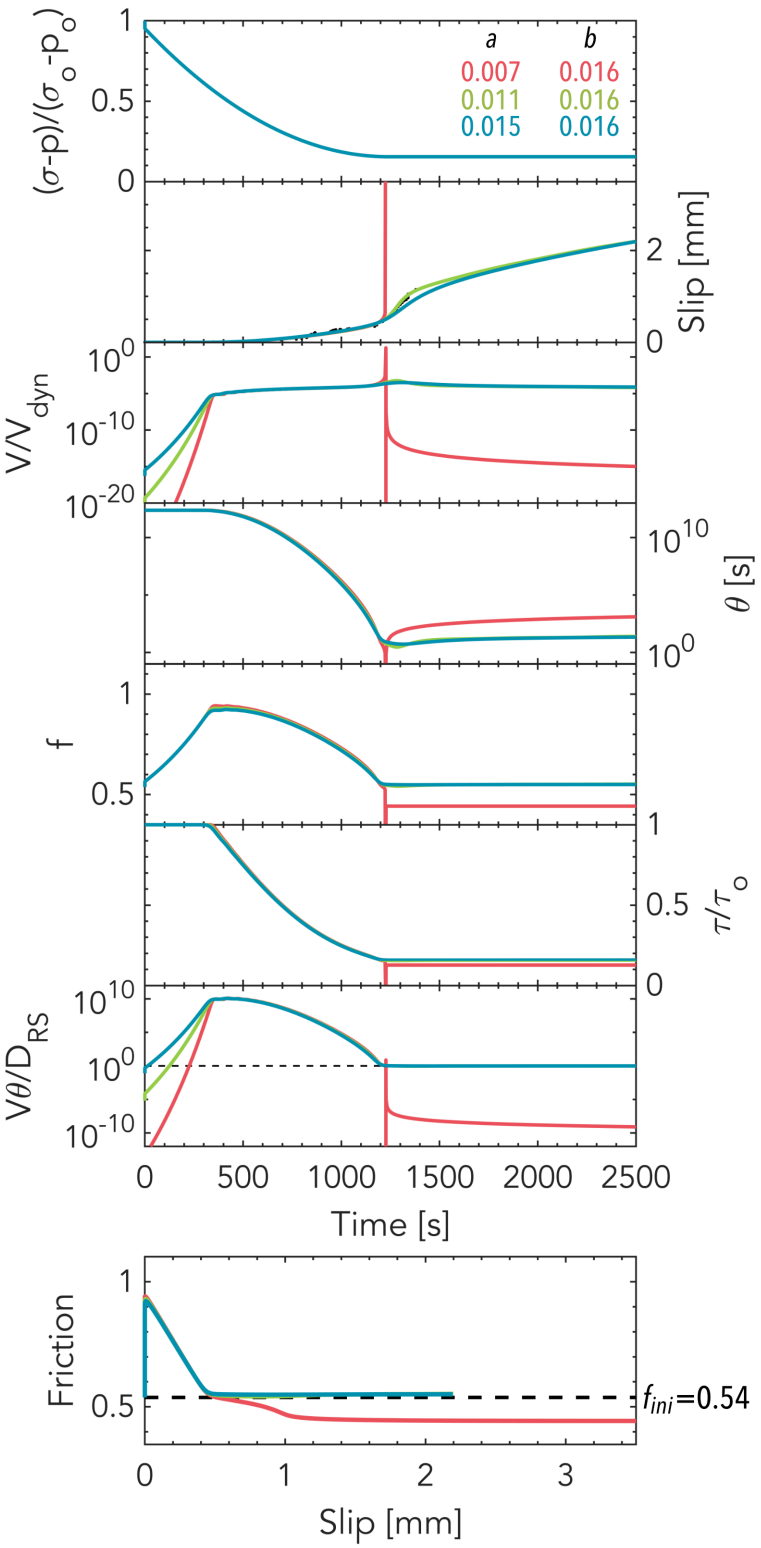

Figure S16. Temporal evolution of quantities at the injection site and friction vs slip of 2 cases showing the effect of varying a. Increasing a reduces the amplitude and slope of the transient acceleration.

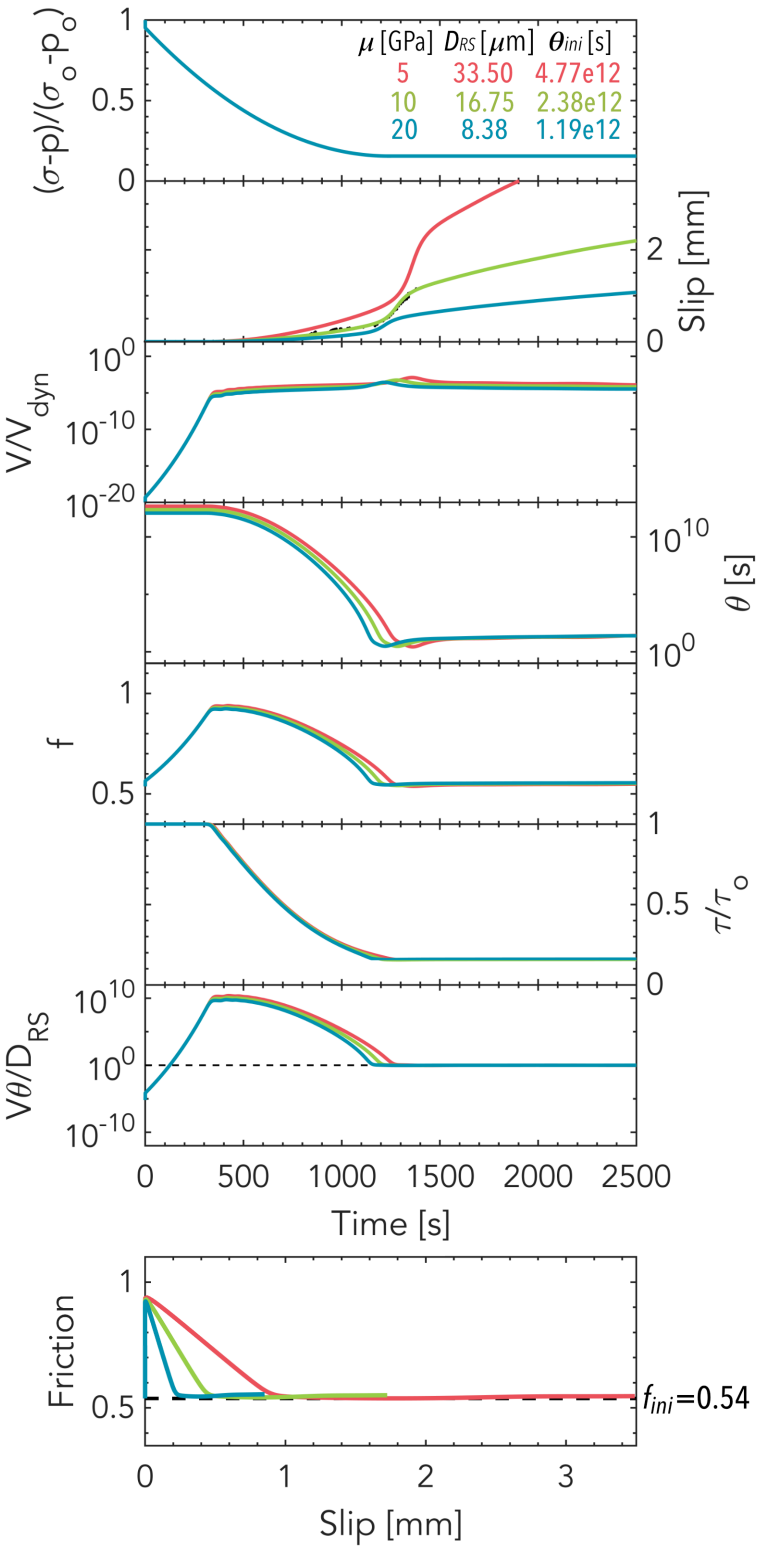

Figure S17. Temporal evolution of quantities at the injection site and friction vs slip of 2 cases showing the effect of varying μ while keeping h_{ac} and f^p constant. Increasing μ reduces the amplitude and slope of the transient acceleration.

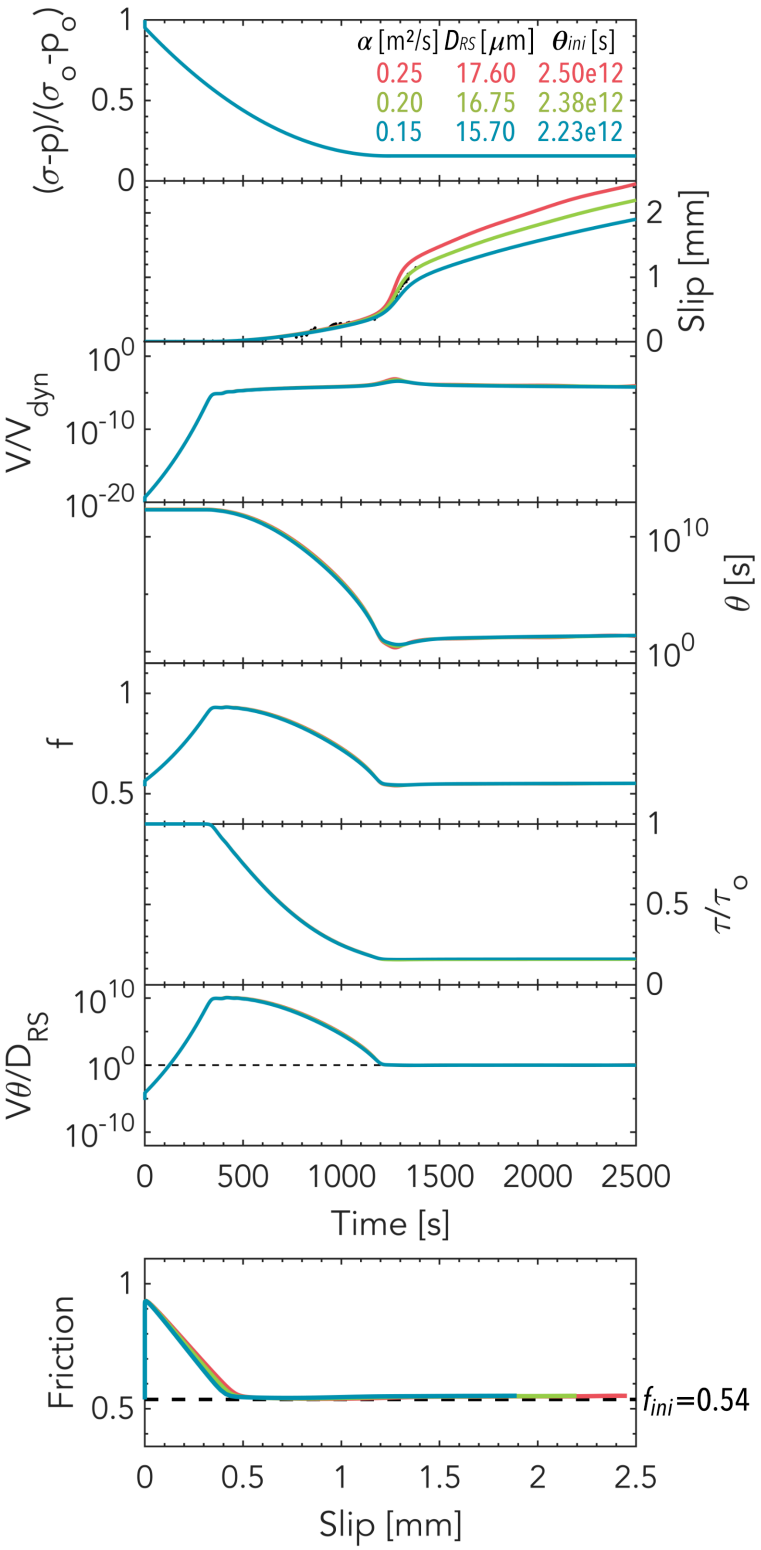

Figure S18. Temporal evolution of quantities at the injection site and friction vs slip of 2 cases showing the effect of varying α while keeping t_{ac} and f^p constant. Increasing α increases the amplitude and slope of the transient acceleration.

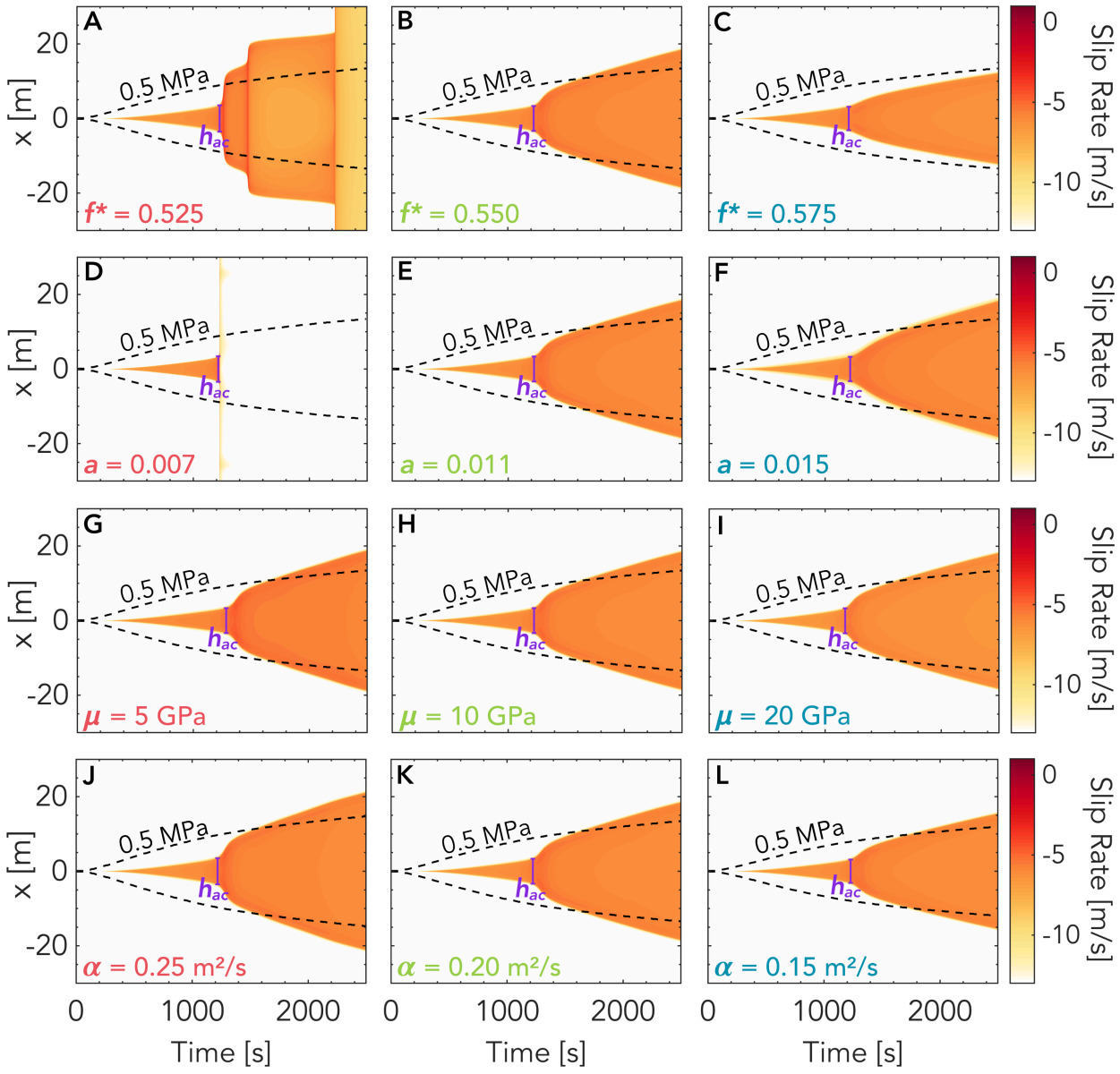

Figure S19. Spatial and temporal evolution of rate for the cases shown in Figures S15 – S18 in which the slope and/or amplitude of the transient acceleration is altered by varying (A,C) f^*, (D,F) a, (G,I) μ and (J,L) α. Panels B, E, H and K all show the reference intermediate-friction case for comparison purposes.

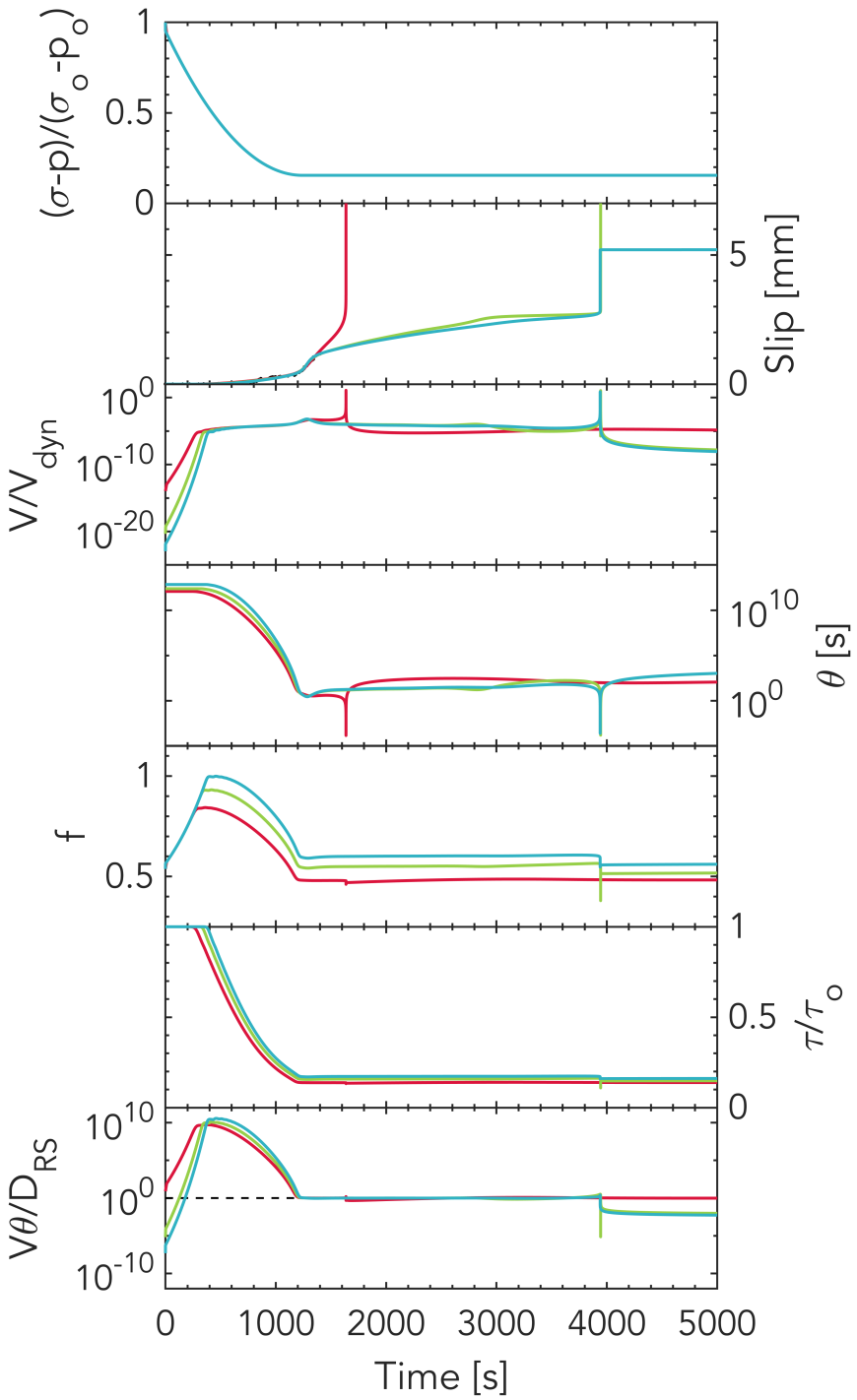

Figure S20. Simulated temporal evolution of several quantities at the injection site for the cases of Figure 4A in the main text. From top to bottom: the normalized effective normal stress, slip, normalized slip rate (V_{dyn} = 10^{-2} m/s), state variable, friction coefficient, normalized shear stress and closeness to steady state at the injection site.

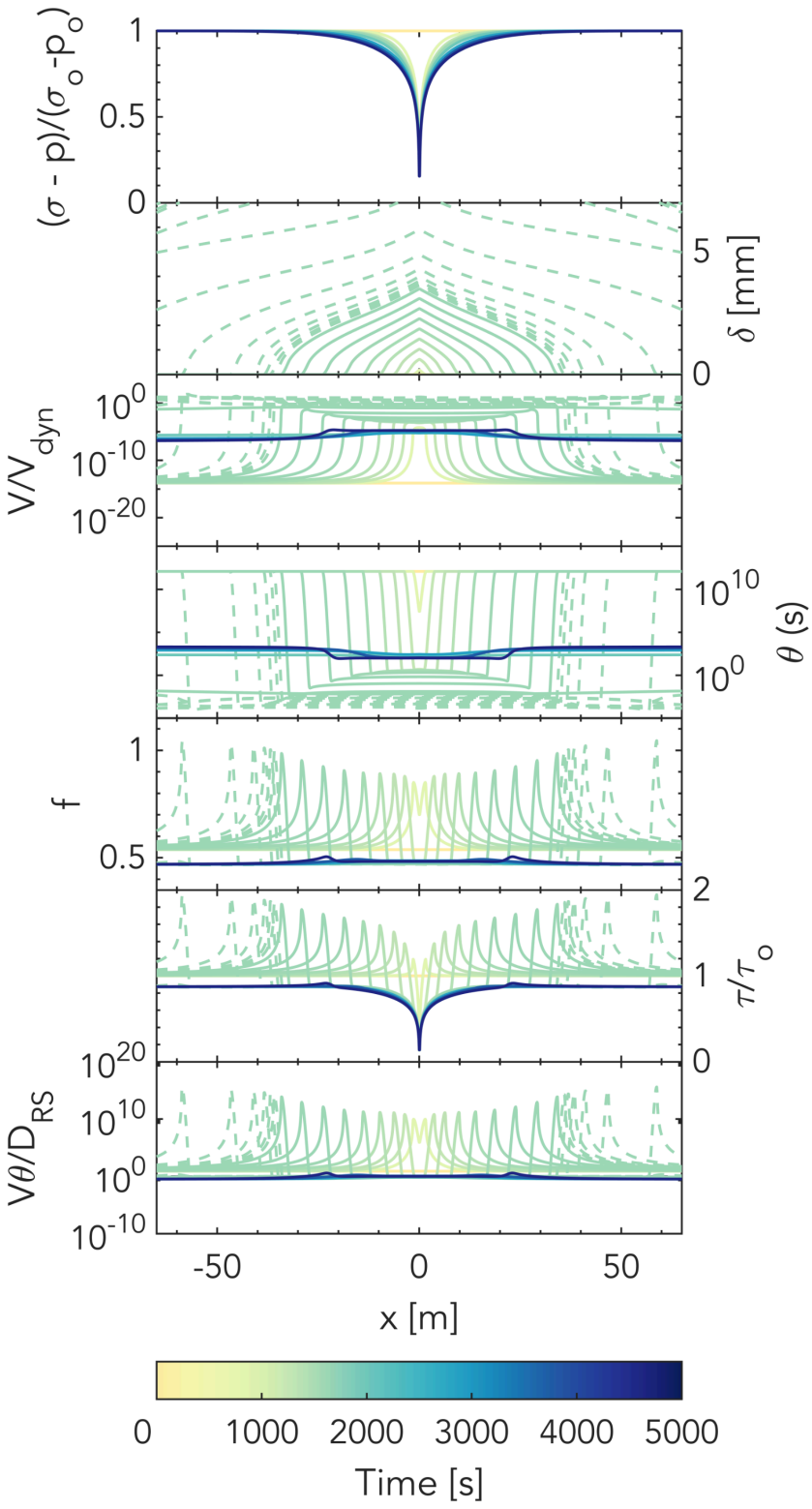

Figure S21. Spatial and temporal evolution of the same quantities as in Fig. S6 for the low-friction prolonged injection case (plotted every 7000 time steps for $V < V_{dyn}$ and every 2000 time steps for $V > V_{dyn}$).

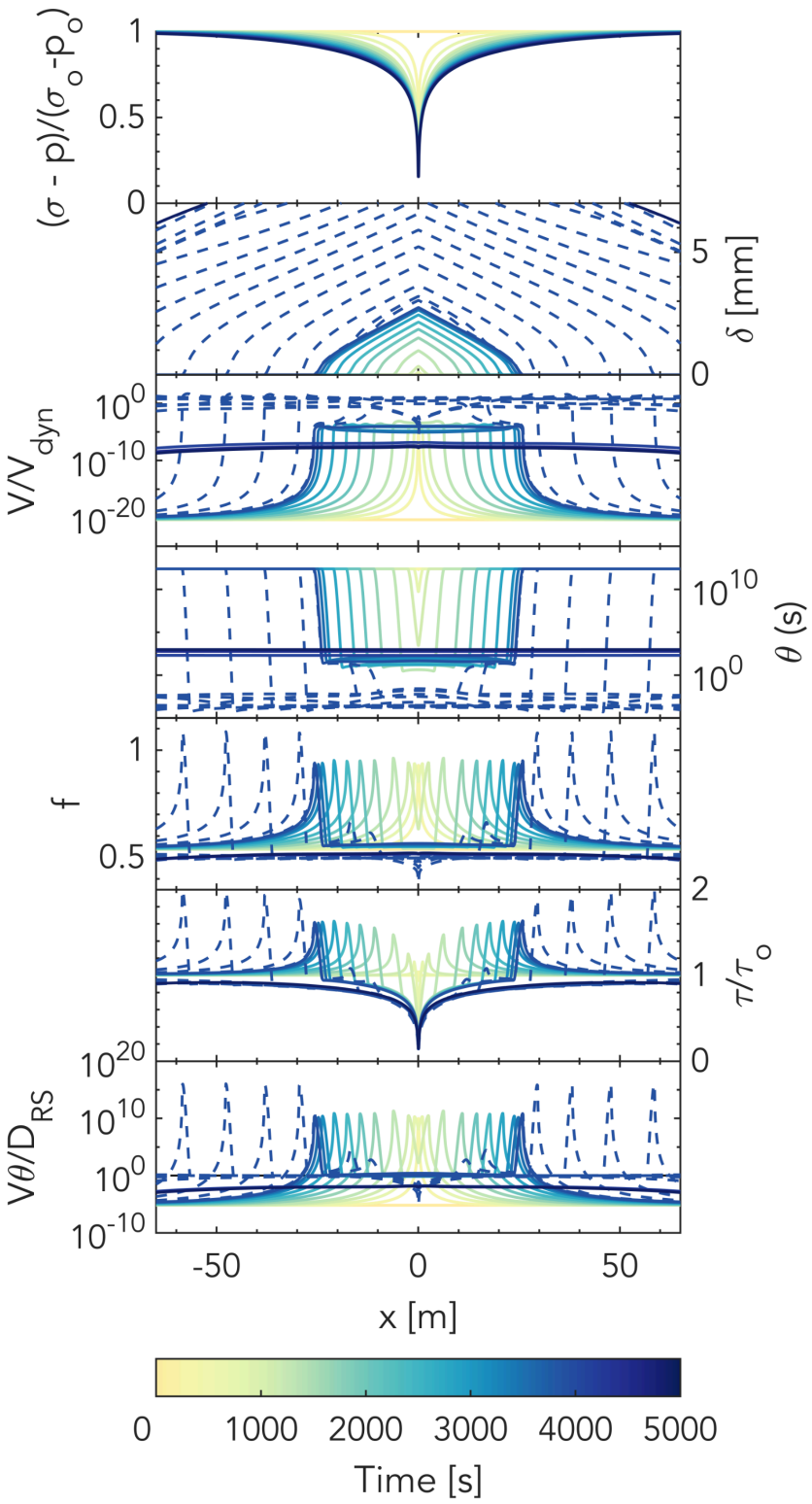

Figure S22. Spatial and temporal evolution of the same quantities as in Fig. S6 for the intermediate-friction prolonged injection case (plotted every 15000 time steps for $V < V_{dyn}$ and every 1000 time steps for $V > V_{dyn}$).

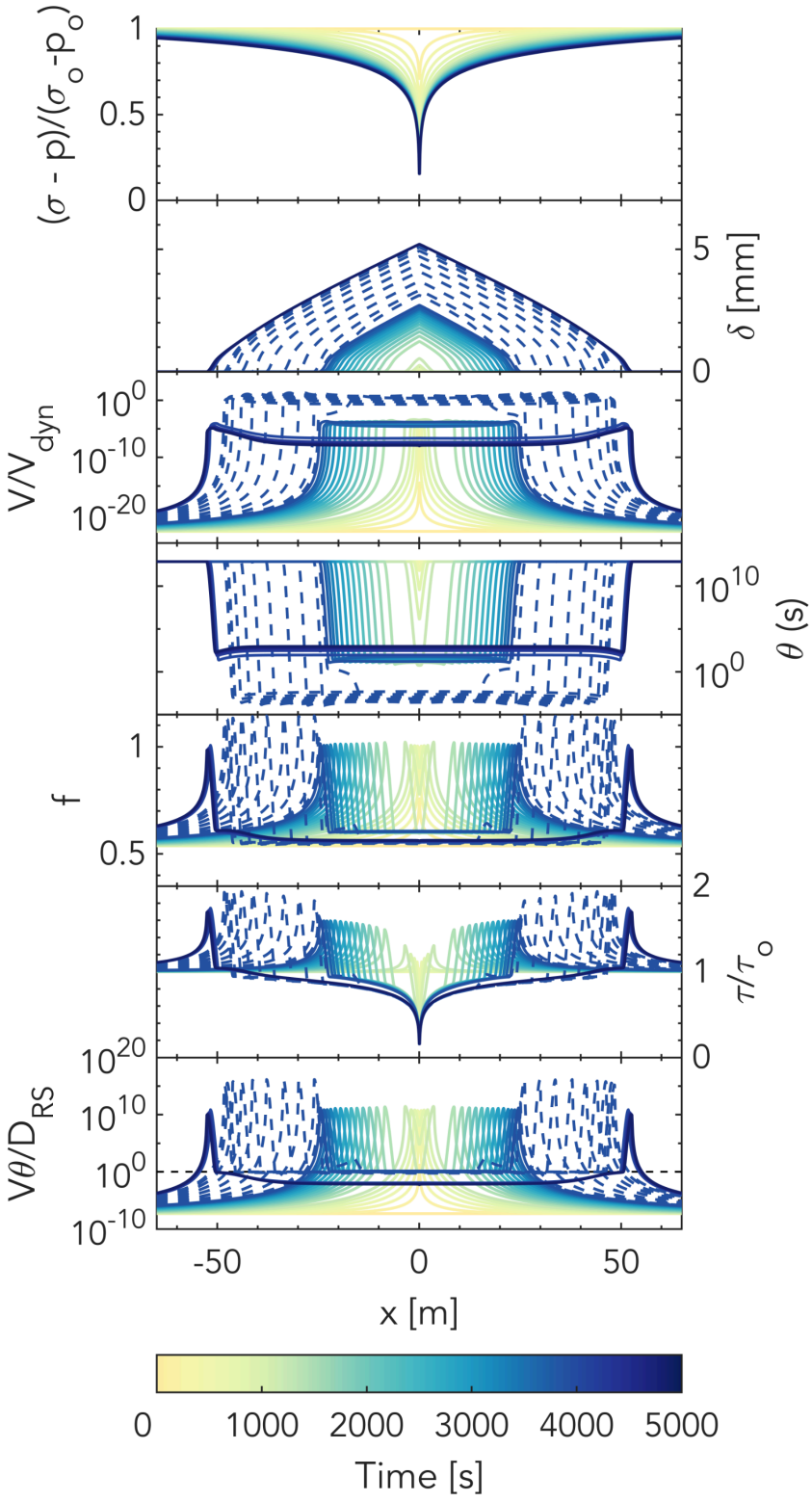

Figure S23. Spatial and temporal evolution of the same quantities as in Fig. S6 for the high-friction prolonged injection case (plotted every 35000 time steps for $V < V_{dyn}$ and every 750 time steps for $V > V_{dyn}$).

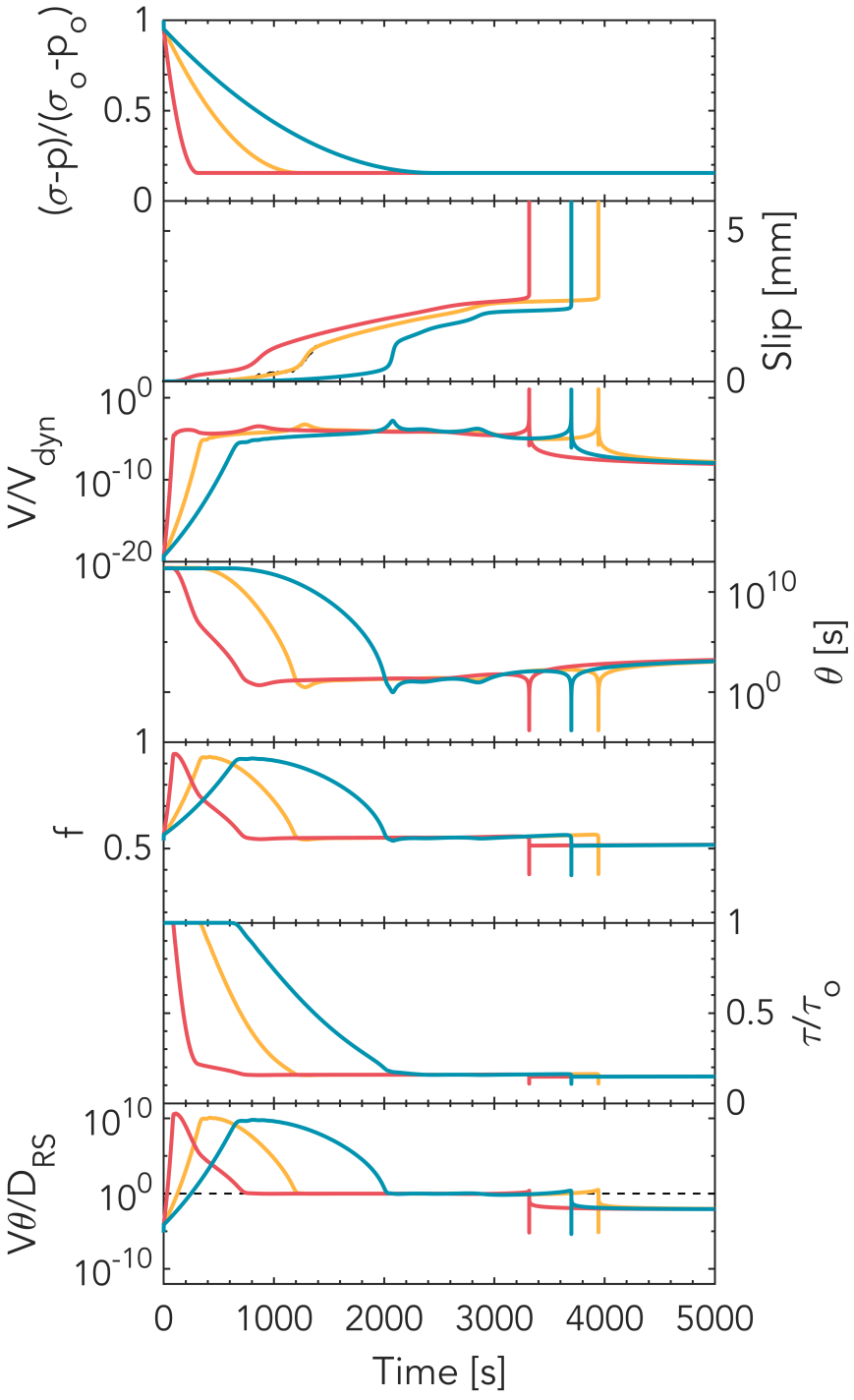

Figure S24. Effect of varying pressurization rate on the intermediate-friction case. The timing of events is altered but not the overall behavior, i.e., all simulations still show a transient acceleration followed by a run-away dynamic event.

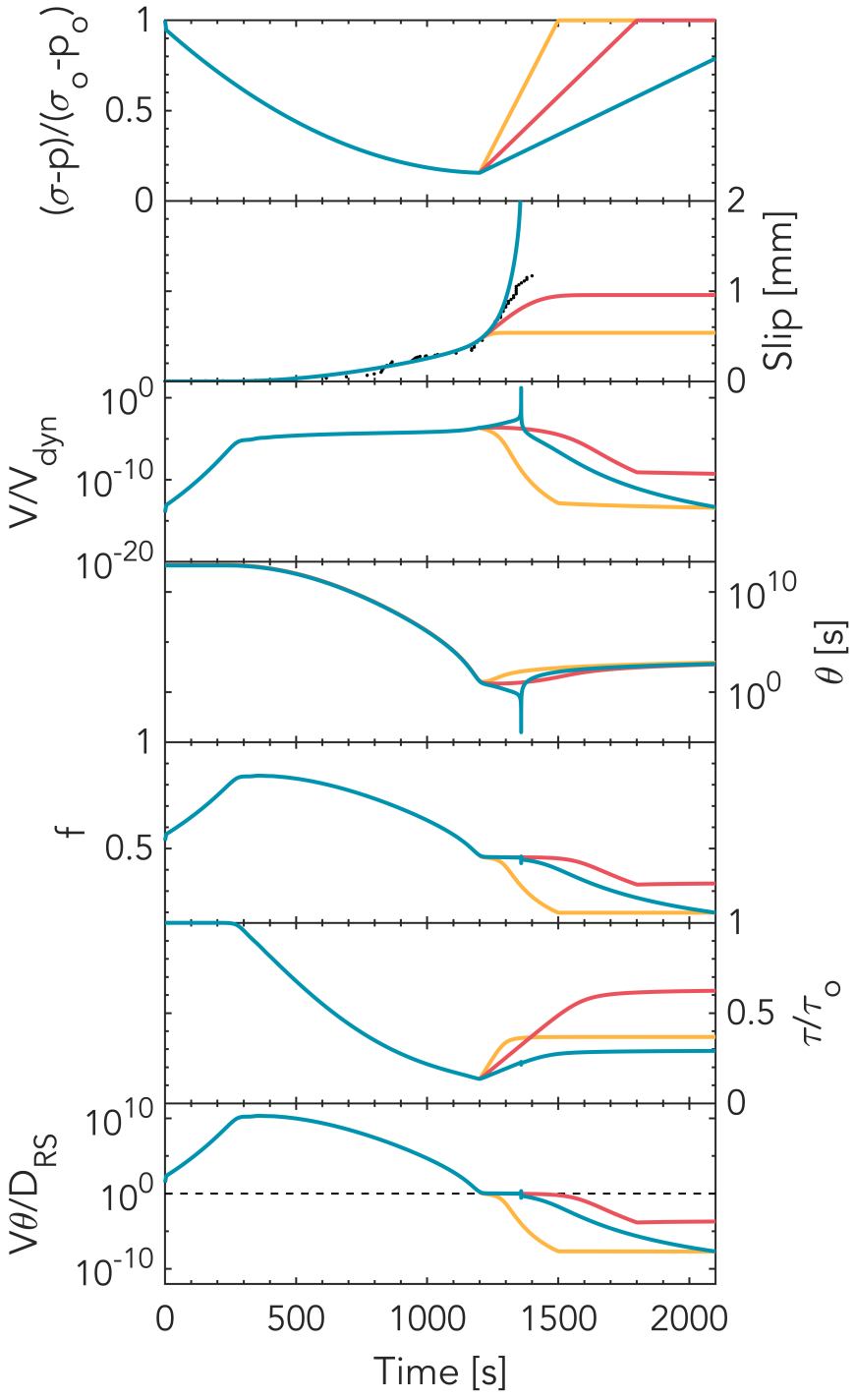

Figure S25. Effect of varying depressurization rate on a case similar to the low-friction case but with an even lower f^* of 0.46. In this case, the depressurization applied as in Figure 2 in the main text is not sufficient to prevent earthquake nucleation (blue curve). The other two faster depressurization rates successfully suppress the earthquake (yellow and pink curves).